Towards transient experimental water surfaces: A new benchmark dataset for 2D shallow water solvers

S. Martínez-Aranda[a], J. Fernández-Pato[a,b], D. Caviedes-Voullième[c], I. García-Palacín[a], P. García-Navarro[a]

[a]*LIFTEC-CSIC, University of Zaragoza, Spain*
[b]*Hydronia Europe, SL*
[c]*Chair of Hydrology. Brandenburg University of Technology, Germany*

Abstract

In the past decade, shallow water solvers have dramatically improved both in terms of accuracy and computational power. New mathematical models and numerical schemes have been systematically verified against 1D exact solutions and laboratory experiments. Despite the two-dimensional nature of some of these benchmark tests, none of them reports complete 2D water depth fields, but only a few profiles are measured and reported in the best case. This work reports a new benchmarking dataset for validation of shallow water solvers, in which two-dimensional transient water depth measurements are available for complex steady and transient laboratory flume experiments, ranging from transcritical steady flow to dam-break flows around obstacles and complex beds. The transient water surface was measured using a commercial-grade RGB-D sensing device which allows to capture a succession of color-coded point clouds at a high frequency. These experimental measurements are compared with 2D shallow water simulations carried out with an extensively tested finite volume solver. Results asses the suitability of this dataset to perform as benchmark tests, identifying potential limitations of current and future models.

Keywords:
Finite volumes, shallow water equations, 3D-sensing, RGB-D sensor, transient free-surface flow

---

Email address: `sermar@unizar.es` (S. Martínez-Aranda)

Preprint submitted to Advances in Water Resources *July 11, 2018*

1. Introduction

Shallow water solvers have received wide attention in the past decade, resulting in a new generation of robust and efficient models [1, 2] in the search for large scale and long term computations of complex transients on both natural and man-made environments. Shallow water models have been extensively benchmarked against test cases, which are widespread in the literature. The solvers have been systematically verified against analytical solutions for simplified problems [3–6]. In addition, they have also been validated against laboratory experiments [7–17], as well as some well-documented real-scale field cases [18–20]. More recently, the experimental literature continues to report transient shallow flows, though with an added interest on sediment transport and moving beds [21–26]

Despite the two-dimensional nature of some of the aforementioned benchmark tests, none of them reports 2D transient water surface elevations. At best, transient data along a few profiles are reported and, more often, transient data are only reported at a few points. Moreover, in field cases, fully transient data are seldom available. Well-established instruments such as pressure gauges [9, 13], ultrasonic gauges [17, 22, 24, 27] and electrically resistive rods [28] have been often used to measure water depth evolution at discrete points. However, in order to capture a 2D transient field, too many of these instruments would be required, making the experimental setup cumbersome, impractical and expensive, without still really achieving high spatial resolution. In 1D flumes, this problem has been solved by using longitudinal imaging [14, 16, 22, 29, 30]. In some cases PIV/PLIF techniques have been used to obtain velocity fields [13, 31, 32]. Additionally, in experimental fluid mechanics, measuring the evolution of a free surface has received little attention, as it has been mainly understood as a problem for shallow water flows and more recently for free surface granular flows [33–35].

As numerical models have become more sophisticated, more complex flow phenomena can be, in principle, accurately simulated. Perhaps some of the most challenging are fast transcritical transients over complex topography and obstacles. These are flows of great interest in Civil Engineering, urban flooding, and risk management in general [36]. It is therefore highly relevant to formally verify that numerical models can indeed reproduce such flow phenomena. The lack of 2D transient experimental measurements generates a gap in model validation.

The unavailability of 2D transient datasets comes from the inherent difficulty of measuring a fast moving water attempting to fully cover the flow field. This is a task for which optical methods are best suited. Refraction-based reconstructions [37–39], stereophotography-based measurements [37, 38, 40, 41], photogrammetry-based methods [42, 43] (although restricted to steady flows), light absorption methods [44, 45], stereo-correlation [46], stereo-refraction [47] and twin-camera refraction analysis of reflected laser light and PIV [48] have all been tested in attempts to capture moving water surfaces, each with their inherent drawbacks on requiring projected referenced grids, specific lighting, sophisticated and expensive equipment, and technical challenges in their setup and processing.

Recently, a wide range of low-cost 3D sensors have appeared as a consequence of the videogame industry development, which are henceforth termed RGB-D (red-green-blue-depth) sensors. The original devices – Carmine (released by Primesense) and Kinect (released by Microsoft in 2010) – were designed to capture human body movements for interaction with video games. The massive size of the videogame market enabled these sensors to be developed and mass produced at a per-unit cost far below that of time-of-flight (ToF) cameras with comparable aquisition frequencies. These low-cost sensors were quickly adapted to new applications such as interactive 3D modelling of indoor environments [49], autonomous flight [50], fluid dynamics measurements [51] or simultaneous location and mapping [52]. The early RGB-D devices were based on the structured-light principle. This approach is an active stereo-vision technique. A set of known patterns, sequentially projected onto an object, gets deformed by the geometric shape. The object is then observed with a camera from a different direction. By analysing the distortion of the observed pattern, i.e. the disparity from the original projected pattern, depth information can be extracted.

Metrological studies have extensively documented the accuracy and usability ranges for such devices [53–55], showing that the depth-accuracy of RGB-D sensors strongly depends on the distance to the measured objects, decreasing quadratically at a short range (4-6 m) [53]. On the other hand, low-cost ToF based sensors such as Kinect2 perform better for the conditions [54]. [56] compared the Kinect device to several ToF devices in a robotic-vision context concluding that they all deliver similar framerates and that both the Kinect and some ToFs achieve lower depth-accuracy than high-grade industrial instruments, although the Kinect outperformed some ToF systems in the short ranges. [57] tested several ToF devices, reporting their maximum framerates, which range between 30-60 fps, putting the Kinect sensor in the lower end of acquistion rates of ToF cameras. When capturing complex objects, [58] showed that low-cost RGB-D sensors are below the accuracy of standard photogrammetry tools, together with other limitations in terms of field-of-view. [59] compared a Kinect sensor to a LiDAR device when capturing 3D cave features, noting again that the Kinect underperforms compared to LiDAR, though still highlighting its ease-of-use and very low cost compared to the high-end instruments. Altogether, the literature suggests that the main limitations of RGB-D devices are depth-accuracy (as compared to ToF, or laser-ranging devices) and their relatively short operational range of distances. Additional practical limitations have been identified, such as limited capability to measure on surfaces with low reflectivity [60, 61] – although this has also been reported to be an issue for some industry-grade ToF sensors [62]–, or infrared-absorbing surfaces [63], excessive background illumination [61], high ambient infrared [63] and the inability to capture data from surfaces nearly parallel to the optical-axis [60, 61]. Moreover, because of their extended use and their low-cost manufacturing, these devices suffer from technical issues such as low thermal stability [63, 64] although, arguably, the errors introduced may be acceptable for many applications. In contrast, it has been argued that ToF devices may suffer from motion artifacts (if there is indeed movement in the images), relatively low resolution, they are more expensive and require somewhat more power, setup and equipment to operate [56, 60, 62].

The obvious advantage of RGB-D sensors, compared to conventional stereo vision cameras and time-of-flight sensors, is clearly their very affordable cost, which makes them an attractive tool for many researchers despite the aforementioned limitations. Researchers have obtained results of enough accuracy using these sensors in fields such as coastal mapping [65], soil and sediment characterisation [66–68], indoor ambient reconstruction [69], plant phenotyping and sizing [70–72] and to obtain dynamic measurements [73, 74].

A few pioneering studies using RGB-D sensors have been reported in Hydraulic or Fluid Mechanics applications. [75] showed the feasibility of capturing moving opaque water surfaces with a Kinect device. [35] measured the transient dynamics of a fast-moving granular surface with a Carmine device. [76] measured surface water gravity waves in clear water in a flume, as a proof-of-concept that refraction can be used for such purposes. In the same line, [77] measured submerged bathymetry with a Kinect device and [78] used a Kinect device to measure the movement of sediment surfaces submerged in clear water, by introducing a refraction correction and to measure the breach morphologic evolution of a failed earth dam [79]. Tests have also been performed with submerged devices [80]. The trend in the literature suggests that it is in fact possible and convenient to measure dynamic water surfaces with RGB-D devices by capturing a seeded flow motion of the water surface or by creating an opaque flow [40].

In the light of this, we present a novel set of transient free-surface water flow experiments with complex geometries, with flow conditions ranging from steady transcritical flows to dam-break cases. In all cases we report the 2D temporal evolution of the water surface captured by means of a commercial-grade RGB-D device measuring opaque water. The aim of the study is to provide a novel and accessible experimental transient water surface dataset. It can serve as benchmark test for current and future generations of 2D shallow water models, both to validate their capabilities and help identify the next set of challenges to be solved. We also point out that this is the first application –to the authors knowledge– of RGB-D sensors for the measurement of complex transient shallow water dynamics.

The paper is organised as follows. The description of the experimental setup and methods, hydraulic setups and postprocessing procedures are presented in Section 2. Section 3 is devoted to the mathematical model used in this paper to provide a quantitative characterization of the data set capability to work as benchmarking tool, as well as the model calibration. Section 4 reports the experimental results. The main features observed in the measured 2D water depth fields for each test are described and compared with the numerical predictions. Finally, in Section 5 some conclusions are drawn.

2. Experimental tests program

2.1. Experimental setup and methods

The experiments were performed on a $6\,m$ long rectangular cross-section $(240 \times 150\,mm)$ plexiglass flume, connected to an upstream reservoir. In the channel reach of interest, the slope was designed to be zero, although measurements reveal a slope of $0.00092\,m/m$ in the first $326\,cm$. Downstream, a bed kink leads to a flume slope of $0.0404\,m/m$, so as to force supercritical flow downstream the measurement region (Fig. 3). A closed circuit allows to establish steady state flow in the flume, and a pneumatically-actuated gate in the upstream boundary allows to generate dam-break conditions with different water elevations in the upstream reservoir. The downstream boundary was always a free outfall into a recirculation tank.

A number of obstacle configurations were placed in the flume which, combined with different steady inflows or dam-break conditions, generated complex 2D water surfaces. The water surfaces were recorded using a consumer-grade RGB-D sensor. The device was suspended 0.7 m above the flume, a good compromise between field-of-view, 2D resolution (millimeters-per-pixel) and depth-accuracy [35, 53, 69]. A generic setup is shown in Figure 1.

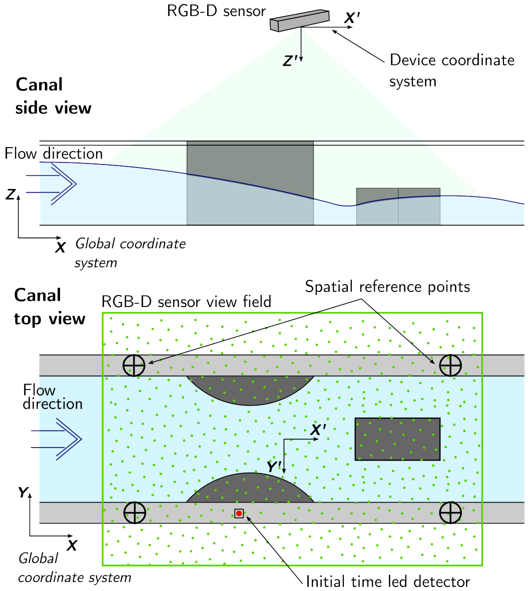

Figure 1: Experimental setup

The different experiments were measured using two different sensors (Primesense Carmine 1.09 and Microsoft Kinect for Windows SDK 1.8). Both devices provide a sequence of $640 \times 480\,px$ RGB + depth-coded images. In short, the devices project standard structured light (SL) into an infrared pattern (by means of NIR laser diode at 850 nm wavelength) onto the objects. The apparent pattern deformation due to the position and shape of the objects is recorded by a monochrome NIR camera observing from a slightly different angle. The apparent deformation allows the devices to produce –in hardware– a depth map for the VGA image. The device streams both the RGB and depth-coded VGA images. They were recorded with Skanect on a laptop computer with a frame-rate of 30 fps approximately. However, actual acquisition frequency depends on additional processes which are computer-dependent, ranging from hardware limitations (mainly regarding sufficient memory to buffer the streams and disk-dumping speed) to OS-prioritised processes. It should be noted that for our rather short experiments the memory buffer was sufficient (32GB) and data were dumped onto a solid-state drive to maintain the highest speed possible. Nonetheless, in practice, the streams were captured with frame-rates from 10 to 30 fps. Captured images were timestamped with millisecond resolution, from which it was possible to study acquisition frequency, and lost frames therefore did not affect the timeline reconstruction. For transient cases, it is of particular interest to register the gate actuation time. This was done by placing a LED on the flume structure within the field of view of the RGB-D sensor. The LED was switched-on when the gate was actuated, allowing to register the time of gate actuation and the duration of gate-opening or gate-closing. The LED lighting was detected in the image by a Matlab script which then time-stamped the image sequence accordingly. In order to easily georeference the flume section and the location of the obstacles, six spatial reference points were placed on the flume structure within the field-of-view of the sensors (three points at each side of the flume).

The devices used project a SL pattern which, in order to observe the water surface, needs to be reflected by it. The transparent nature of water does not allow for this. A simple solution is to tint water until it is opaque and reflects the pattern at the surface. A proof-of-concept of this was reported by [75] and used with stereophotography by [40]. In the present work, water was tinted with titanium oxide (TiO_2) at a concentration of 1.2% in mass. This allows to reflect the pattern off the water surface, thus not requiring reflection corrections as proposed by [76, 78]. It also has the advantage that the white color of the water allows for visual color contrast with the obstacles and channel bed. In addition to the transient flow surfaces, the flume bed and obstacles were also captured with the RGB-D in a dry condition, to completely characterise the channel bed within the field of view.

2.2. Tested cases

Four different geometrical configurations were set using a floor bump ($20.1\,cm$ radius, $31 \times 24\,cm$ footprint, $7.3\,cm$ maximum height), lateral Venturi constriction elements ($20.1\,cm$ radius, $31\,cm$ long, $15\,cm$ height and $7.3\,cm$ maximum width), a rectangular obstacle ($16.3x8.0x7.0\ cm$) and a bridge structure. All elements, except the bridge structure were constructed out of PVC. The bridge structure was constructed from Styrene sheets.

The four configurations are next presented:

1. **G1**: Rectangular obstacle placed at the center line of the flume, as shown in Figure 2.

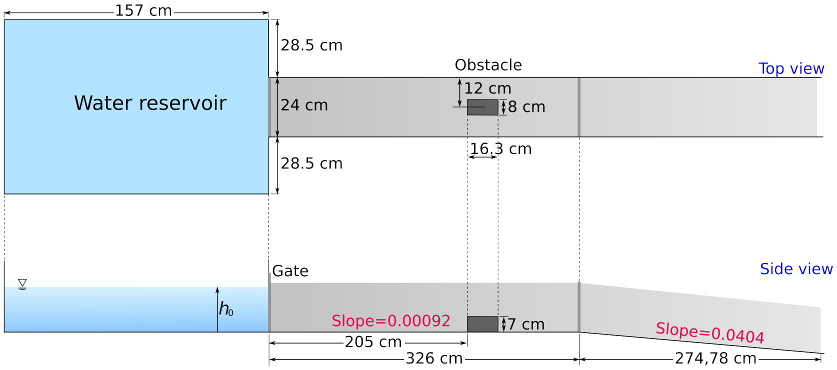

Figure 2: G1 configuration: centered obstacle

2. **G2**: Floor bump across the entire flume width followed by a rectangular obstacle placed at the center line of the flume, as shown in Figure 3.

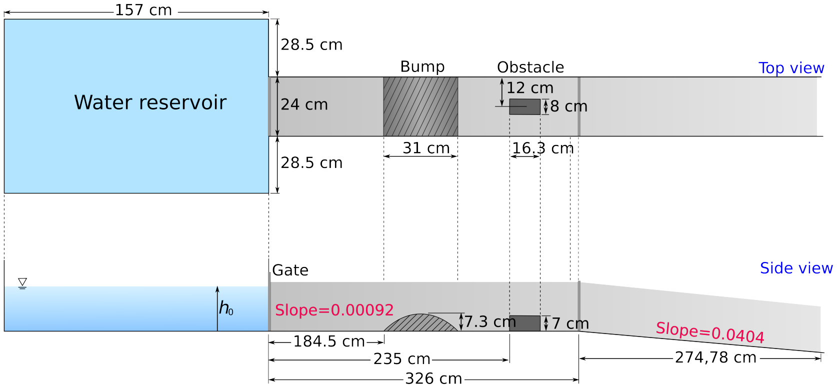

Figure 3: G2 configuration: bed bump and centered obstacle.

3. **G3**: Venturi narrowing and a rectangular obstacle downstream, as shown in Figure 4.

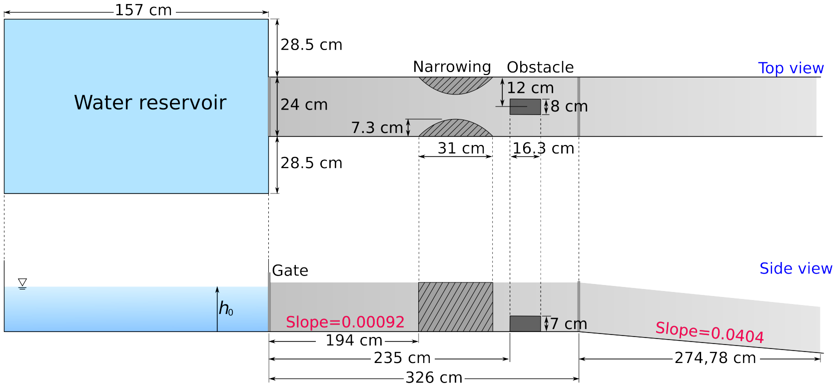

Figure 4: G3 configuration: Venturi narrowing and centered obstacle.

4. **G4**: Bridge structure with two arches. The arches were 8 cm wide and 5 cm high at the center. Downstream the bridge two slender rectangular obstacles were placed, one of them following the flume center line (19.2x1.0x3.5 cm) and the other obliquely to the flume wall (9.5x1.5x5.0 cm and 21^o respect to the flume wall), as shown in Figure 5.

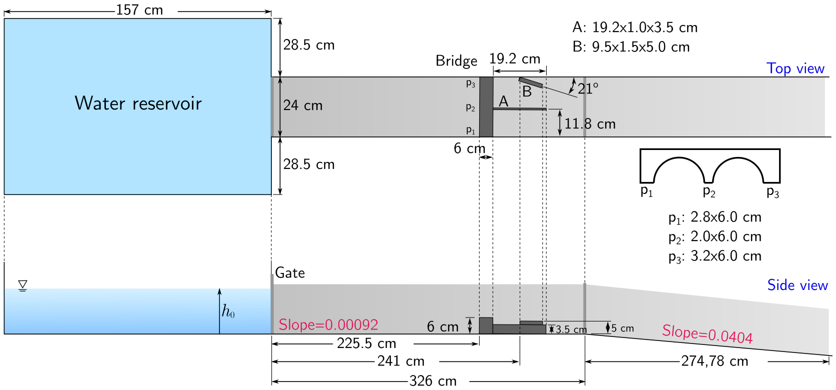

Figure 5: G4 configuration: two-arch bridge with downstream obstacles.

The aforementioned geometry configurations were used for various steady and unsteady flow conditions which are summarised in Table 1, totalizing eleven experimental tests. Steady cases were performed setting a constant discharge in the flume. For dam-break cases the reservoir was filled to a height h_0 above the flume floor. Then the gate was suddenly open and the water free-surface was captured with the variable frequency provided by the RGB-D sensor. The gate opening time was determined from the indicator

LED light placed in the sensor view area and it was set as the initial time for measurements.

Geometry	Regime	Name	Discharge $[m^3/h]$	Gate depth $[cm]$	Device
G1	Steady	G1-S.1	5.05	-	Kinect
		G1-S.2	9.01	-	Kinect
		G1-S.3	12.05	-	Kinect
	Dam-break	G1-D.1	-	5.5	Kinect
G2	Steady	G2-S.1	5.05	-	Kinect
		G2-S.2	9.01	-	Kinect
	Dam-break	G2-D.1	-	13.0	Kinect
G3	Steady	G3-S.1	5.05	-	Kinect
		G3-S.2	9.01	-	Kinect
	Dam-break	G3-D.1	-	5.5	Kinect
G4	Steady	G4-S.1	5.75	-	Carmine

Table 1: Summary of experimental cases

2.3. Post-processing

The raw data recorded with Skanect were treated with an ad-hoc C code based on the open-sourced PCL library together with an ad-hoc Matlab script. The raw depth-maps were processed into 3D point clouds and then projected into a constant 2D structured grid (a raster, essentially) in order to obtain operable data sets for the free-surface elevation. For steady cases, the discharge in the channel was controlled and the obtained 2D water depth fields were averaged in time. In unsteady cases, a dam-break wave moves through the initially dry measurement area. The temporal evolution of the water free-surface field showed the formation and development of complex two-dimensional transient structures.

For steady flow cases, the reported water surfaces were determined from averaging 60 images of the sequence. Water depths were determined for all cases by substracting the topography surface – containing the flume bed and obstacles – from the water surface (averaged, in steady cases; instantaneous, in transient cases).

3. Mathematical model and numerical simulations

In this paper, surface flow is modelled using the 2D shallow-water equations [81, 82], which can be written as:

$$\frac{\partial \mathbf{U}}{\partial t} + \frac{\partial \mathbf{F}(\mathbf{U})}{\partial x} + \frac{\partial \mathbf{G}(\mathbf{U})}{\partial y} = \mathbf{S} + \mathbf{H} \tag{1}$$

where

$$\mathbf{U} = (h,\ q_x,\ q_y)^T \tag{2}$$

are the conserved variables, being $h\,[L]$ the water depth and $q_x = hu$ and $q_y = hv$ the unit discharges $[L/T]$ along the x and y coordinates respectively, with u and v the depth averaged components of the velocity vector $\mathbf{u}\,[L/T]$. The fluxes associated to these conserved variables are

$$\mathbf{F} = \left(q_x,\ \frac{q_x^2}{h} + \frac{1}{2}gh^2,\ \frac{q_x q_y}{h}\right)^T, \qquad \mathbf{G} = \left(q_y,\ \frac{q_x q_y}{h},\ \frac{q_y^2}{h} + \frac{1}{2}gh^2\right)^T \tag{3}$$

where $g\,[L/T^2]$ is the gravity acceleration. The source terms on the right-hand-side of the system are split into two kind of terms depending on the nature of the source. The term $\mathbf{S}$ represents the friction and it is defined as

$$\mathbf{S} = (0,\ -ghS_{fx},\ -ghS_{fy})^T \tag{4}$$

where S_{fx}, S_{fy} are the friction slopes in the x and y direction respectively, here expressed in terms of the Manning's roughness coefficient $n\,[T/L^{1/3}]$:

$$S_{fx} = \frac{n^2 u\sqrt{u^2+v^2}}{h^{4/3}}, \qquad S_{fy} = \frac{n^2 v\sqrt{u^2+v^2}}{h^{4/3}} \tag{5}$$

The term $\mathbf{H}$ accounts for the variation of the pressure force along the bottom in both x and y directions. It is formulated in terms of the bed slopes of the bottom level $z\,[L]$:

$$\mathbf{H} = \left(0,\ -gh\frac{\partial z}{\partial x},\ -gh\frac{\partial z}{\partial y}\right)^T \tag{6}$$

Equations (1) are a depth-averaged model that is only valid under the assumption of negligible vertical accelerations and, therefore, is associated to a hydrostatic pressure distribution. However, it represents a widespread formulation in Hydraulic Engineering. System (1) is non linear, time dependent and contains several source terms. It can be included into the family of hyperbolic systems under the hypothesis of dominant advection. Among the mathematical properties of (1) is the existence of a Jacobian matrix, $\mathbf{J_n}$, of the flux in the outward normal direction given by the unit vector $\mathbf{n}$, $\mathbf{E} \cdot \mathbf{n} = \mathbf{F} n_x + \mathbf{G} n_y$, [83] defined as

$$\mathbf{J_n} = \frac{\partial \mathbf{E} \cdot \mathbf{n}}{\partial \mathbf{U}} = \frac{\partial \mathbf{F}}{\partial \mathbf{U}} n_x + \frac{\partial \mathbf{G}}{\partial \mathbf{U}} n_y \tag{7}$$

The equations presented in this section are solved by a first-order explicit finite volume scheme described in detail by [83]. The numerical model is designed to solve the flow variables only in the wet cells, in order to reduce the computational time. The method is able to work on both structured and unstructured meshes. In the present work examples, unstructured triangular meshes were used in order to be able to fit them to the shape of the obstacles and also to benefit from the possibility of local refinement.

The numerical scheme had been previously proved well-balanced and able to deal with situations of wet/dry fronts, providing stable solutions with a mass error comparable to the machine accuracy [84]. The details of the numerical scheme used are out of the scope of the present work.

3.1. Manning roughness calibration

In order to properly predict the friction term influence in the flow behavior, the Manning roughness coefficients n for the plexiglass flume and the PVC bed bump were calibrated in a first step. Five different steady inlet discharges ($Q_1 = 1.17\, m^3/h$, $Q_2 = 4.01\, m^3/h$, $Q_3 = 7.41\, m^3/h$, $Q_4 = 10.76\, m^3/h$, $Q_5 = 14.06\, m^3/h$) were set and the water depth was directly measured with a rule at different points along the flume center axis. A first set of measurements was performed with a clear flume bed (without any obstacles) in order to estimate the plexiglass roughness coefficient. Then, a second set of measurements was performed placing the bed bump 1.845 m downstream the gate (see Figure 3) and setting the same steady inflows.

Experimental water depth values measured along the longitudinal flume center axis were compared with simulations carried out setting identical steady inflows to that of the experiments and varying the Manning's roughness coefficient n for plexiglass and PVC material between $0.008\, sm^{-1/3}$ and

$0.012\,sm^{-1/3}$. Numerical results showed the best agreement with experimental water depth in the reach of the flume for a Manning coefficient of $0.01\,sm^{-1/3}$, for both plexiglass floor and PVC bed bump. Figure 6 shows the longitudinal water depth profiles with $n = 0.01\,sm^{-1/3}$ and $n = 0.008\,sm^{-1/3}$ for the clean plexiglass flume, in order to justify the selection.

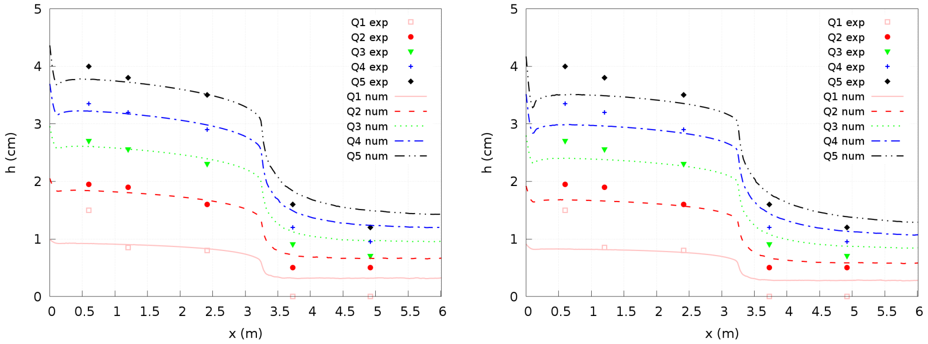

Figure 6: Experimental (points) and numerical (lines) water depth along the longitudinal flume axis with (left) $n = 0.01\,sm^{-1/3}$ and (right) $n = 0.008\,sm^{-1/3}$ for the clean plexiglass flume.

4. Experimental results

4.1. RGB-D sensor validation with direct measurements

As initial test case for the RGB-D sensor measurements, a steady discharge $Q = 11.66\,m^3/h$ was set in the flume with the Venturi narrowing placed at $214.5\,cm$ downstream the pneumatic gate. Upstream the narrowing the flow was subcritical, changing to supercritical at the throat. Downstream the narrowing a supercritical diamond-shape structure appeared, with small water depth values at the flume center. The water depth profile along the longitudinal flume center axis was direct measured each 5 cm (from $X = 205\,cm$ to $X = 275\,cm$) using a rule. Moreover, the water free-surface was captured with the Primesense Carmine 1.09 device and it was processed to obtain the steady 2D water depth field. Figure 7-left shows the reconstructed water free-surface at the narrowing region.

Figure 7-right depicts the water depth profile along the longitudinal flume center axis ($Y = 12\,cm$) for the direct measurements and the RGB-D sensor results. Relative differences in absolute value between both set of experimental data (normalized by the mean flow depth upstream the narrowing) are

also shown in the same figure. The higher differences were found downstream the Venturi, where the flow was supercritical and the water depth values were more limited. Nevertheless, relative differences remained below 10% (of the mean flow depth) along the longitudinal profile.

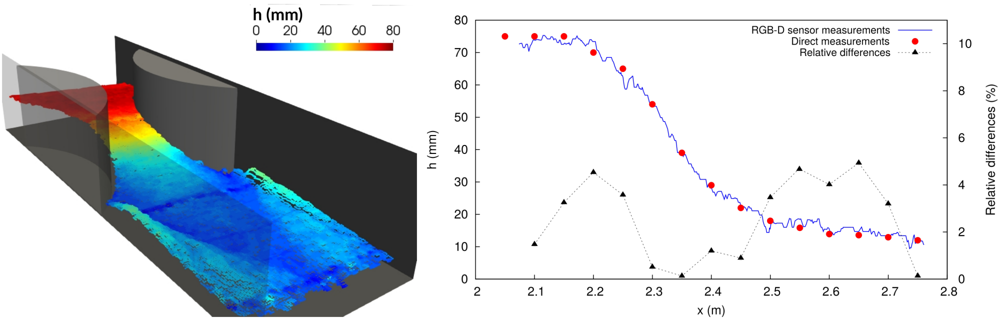

Figure 7: Initial test case. (left) Reconstructed water free-surface; (right) Comparison of RGB-D and direct water depth measurements along the longitudinal flume center axis.

4.2. Centered obstacle (G1)

4.2.1. Steady flow - Cases G1-S.1, G1-S.2 and G1-S.3

Three different steady discharges were used ($Q_1 = 5.05\, m^3/h$, $Q_2 = 9.01\, m^3/h$ and $Q_3 = 12.05\, m^3/h$) with this geometrical configuration. Time-averaged water-depth fields are depicted in Figure 8. Experimental results showed a steady rarefaction wave generated at the upstream face of the obstacle. This wave increased its height as discharge increased. Downstream the obstacle upstream face a complex wave structure was observed with different diagonal shock waves. A symmetric wake appeared downstream the obstacle tail. The position of the different waves did not show significant changes as the discharge increased.

Numerical simulations (Figure 8-right) predicted accurately the flow structure observed in the experiments, especially the upstream frontal rarefaction wave and the diamond wake configuration. Some differences were found at both sides of the centered obstacle, where the numerical model predicted a slightly different flow configuration since the transverse shock wave at both sides of the obstacle appeared slightly upstream in the numerical prediction than in the experimental measurements. Also it can be observed that the water flow surface at the final section is not well reproduced by the numerical model.

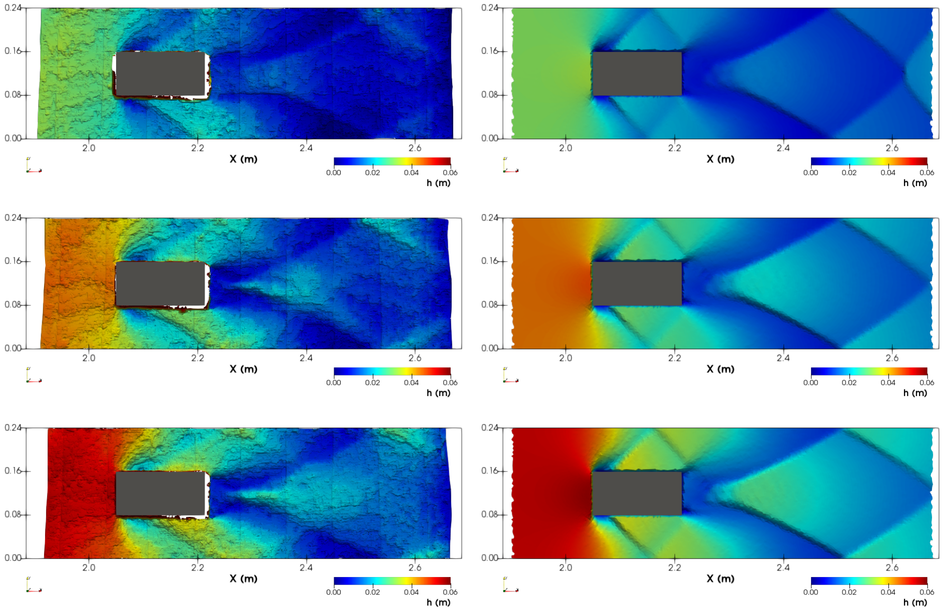

Figure 8: Experimental (left) and numerical (right) water depth 2D-fields for cases (top row) G1-S.1, (center row) G1-S.2 and (bottom row) G1-S.3.

A comparison of measured and simulated water depth profiles along the two longitudinal axis ($Y = 0.12\,m$ and $Y = 0.20\,m$) of the flume and two cross-sections ($X = 2.10\,m$ and $X = 2.30\,m$) is depicted in Figure 9. Larger differences are observed in the obstacle wake close to the field-of-view limit region, and in the immediate neighbourhood of the obstacle. It should be stressed that in the field-of-view ending region the numerical model was able to predict reasonably well the hydraulic jump locations but the water depth was underestimated, especially along the longitudinal $Y = 0.20\,m$. The possibility to obtain any water depth profile (depending on the modeller requirements) is one of the main advantages of the reported experimental data set, compared with other existing benchmarking tests.

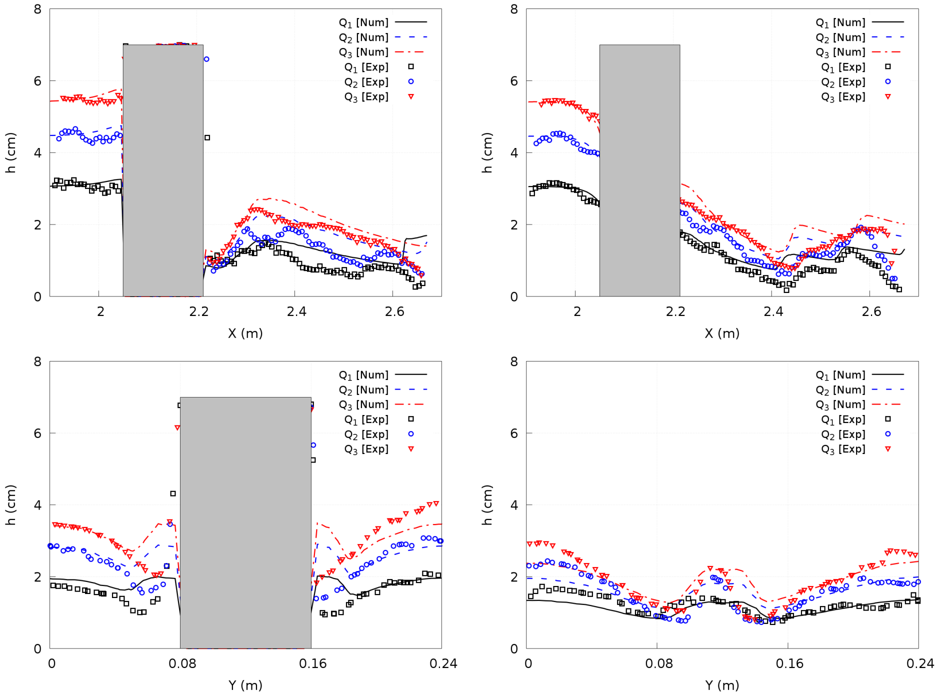

Figure 9: Experimental (dotted lines) and numerical (solid lines) water depth for steady cases with geometry G1. Top row: Longitudinal profiles at Y = 0.12 m (left) and Y = 0.20 m (right). Bottom row: cross-section profiles at X = 2.10 m (left) and X = 2.30 m (right).

The relative differences between experimental and simulated water depth (normalized by the mean flow depth upstream the obstacle region) along the longitudinal profile $Y = 0.12\,m$ and cross-section $X = 2.10\,m$ are also shown in Figure 10. The relative depth difference was higher at the wake center and close to the obstacle's lateral faces. This difference always remained below 20% in the wake region but it increased close to the downstream end of the field-of-view where the measurements may be affected by an excessive optical angle and the reduced flow depth [55]. The cross-section profile at X = 2.10 m showed relative differences below 10% far from the obstacle's sides but it increased close to them (35%). This increment was mainly caused by the disagreement in the oblique shock wave position between experimental measurement and numerical prediction, as it was commented above. Experimental errors exist around the obstacle sides due to shading and high-sloping water surfaces. This is due to having a single sensor with a vertical optical axis meaning that certain regions around obstacles and vertical surfaces are occluded. This can of course be alleviated by placing more sensors, with different fields-of-view and perhaps different optical axis. Simulated results may also be inaccurate due to shallow-water model assumptions breaking in the immediate neighborhood of the obstacle. Moreover, the lack of symmetry in the numerical profiles is due to the use of an unstructured triangular mesh. In summary, high errors in such close range of the obstacle are to be expected, and are difficult to attribute solely to either experimental or numerical issues.

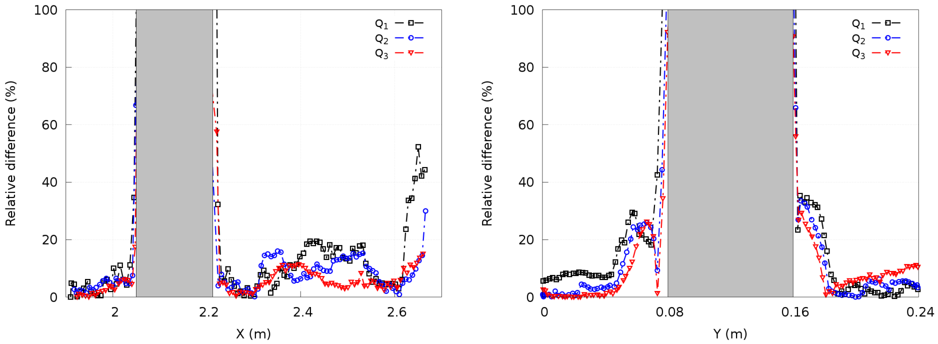

Figure 10: Relative differences between experimental and numerical water depth for steady cases with geometry G1: (left) longitudinal profile at Y = 0.12 m and (right) cross-section at X = 2.10 m.

4.2.2. Dam-break flow - Case G1-D.1

A dam-break case was performed in the flume by setting an initial water depth upstream the boundary gate of $h_0 = 5.5\ cm$ above the flume bed. The gate was suddenly opened and the actuation time t_0 was captured by the indicator LED light. The time necessary to open the gate was $500\,ms$ approximately. Figure 11 shows a time sequence of the 2D water depth field for the Kinect data (left column) and the numerical results (right column). The dam-break wave propagated downstream through the flume reach of interest until it reached the centered obstacle at $t \approx 2.6\ s$. A shock wave developed upstream the obstacle, initially increasing its depth with time. The shock wave bended symmetrically around the obstacle, taking a slightly curved shape, concave in the downstream direction ($t = 3.051\ s$) which later developed into a downstream-oriented diagonal front. Upstream the obstacle the shock wave developed into a hydraulic jump fully perpendicular to the main flow direction ($t = 3.863\ s$) which propagated upstream until it was dissipated at the boundary reservoir. Downstream the obstacle a narrow diamond wake was formed, similar to the steady cases ($t = 3.301\ s$).

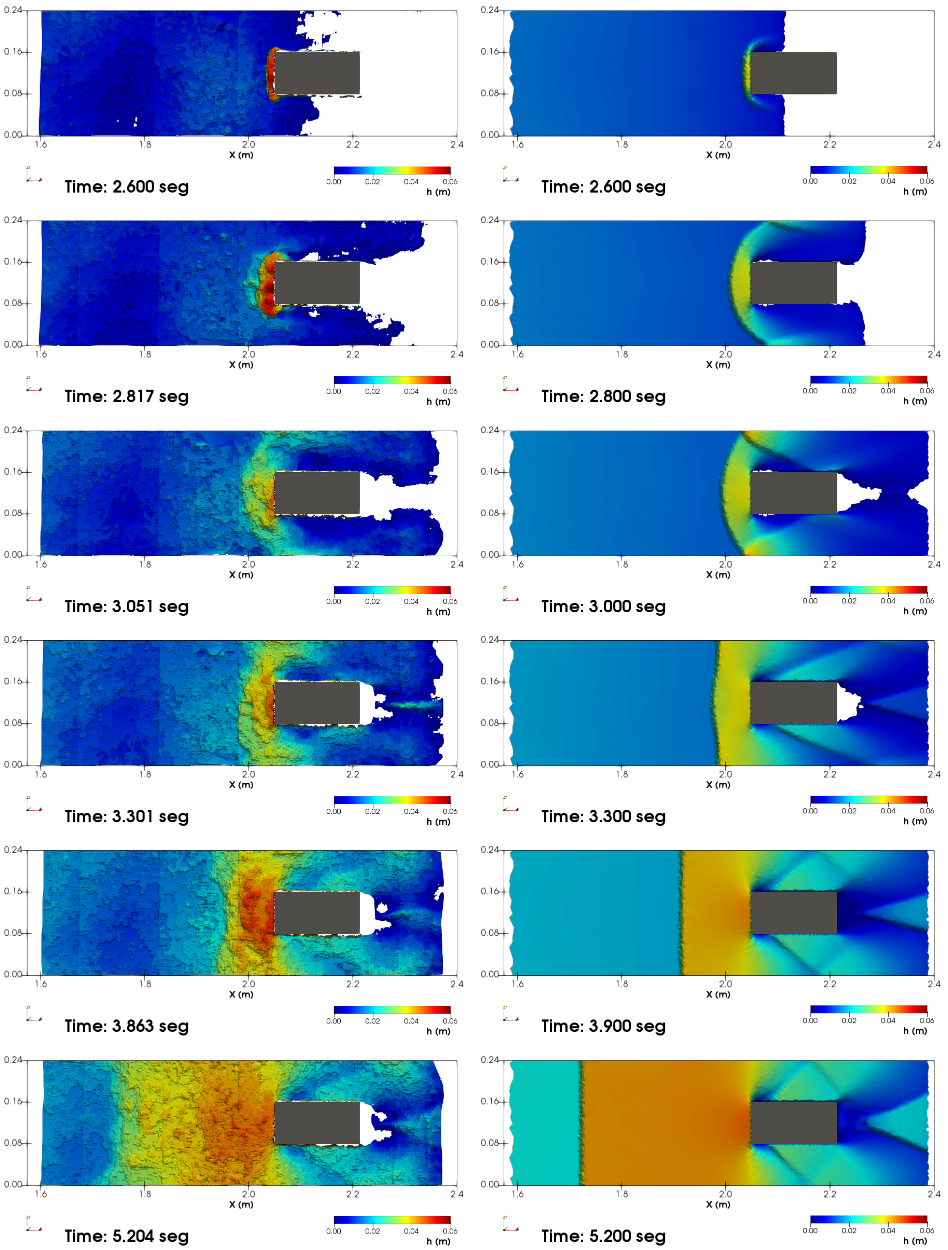

Figure 11: Experimental (left column) and numerical (right column) water depth 2D-fields for case G1-D.1 at different times.

The numerical model accurately predicted the dam-break wave arrival time and the development of the shock wave upstream the obstacle. Furthermore, the temporal evolution of the computed free surface showed a suitable agreement with what was observed in the laboratory, especially for the frontal hydraulic jump appearance and evolution. Differences between the measured and simulated free surface structure appeared, in particular for the upstream shock wave generation process ($t \leq 3\,s$). Flow around and downstream the obstacle was well predicted by the numerical model. Wake structures and their opening angles were well captured.

Figure 12 depicts the temporal evolution of water depth along the flume longitudinal axis ($Y = 12\ cm$) and a longitudinal profile located equidistant from the left flume wall and the obstacle left face ($Y = 20\,cm$). The numerical water depth profiles show a good agreement with the experimental data, although the hydraulic jump position is not well captured.

These line snapshots are examples of the kind of information that can be extracted from the dataset straightforwardly. On the other hand, it is worth noting that the representation of time evolution at a probe is more complicated as it requires an ad-hoc post-processing of the data.

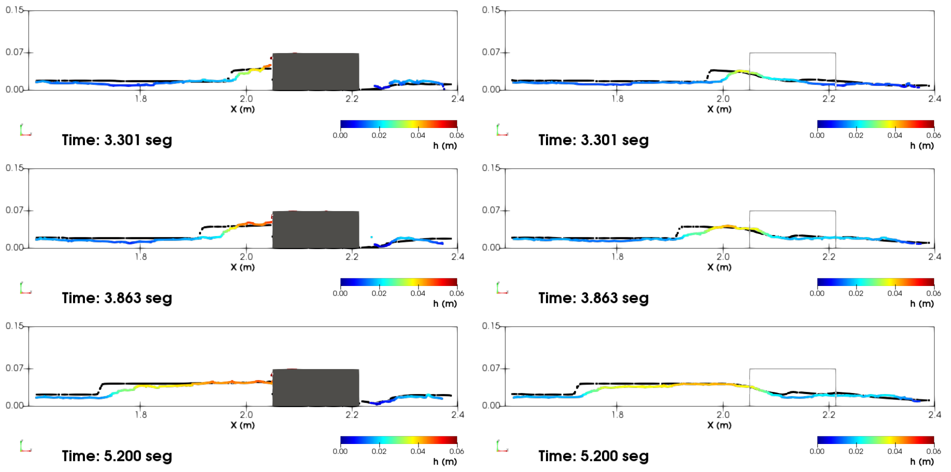

Figure 12: Experimental (coloured line) and numerical (black line) free-surface longitudinal profiles for case G1-D.1 at different times: (left column) Y = 12 cm and (right column) Y = 20 cm. Grey color line represent the bed bump.

4.3. Floor bump and centered obstacle (G2)

4.3.1. Steady flow - Cases G2-S.1 and G2-S.2

For this geometry, two different steady inflow discharges were set ($Q_1 = 5.05\,m^3/h$ and $Q_2 = 9.01\,m^3/h$). Experimental time-averaged water depth fields are depicted in Figure 13-left. The flow was subcritical upstream the bump for both tested discharges and it became supercritical downstream the bump. The flow velocity increased in the transcritical region over the PVC floor bump, resulting in a very low water depth difficult to measure with traditional experimental techniques. A slightly marked and curved shock wave appeared upstream the obstacle for a discharge of $5.05\,m^3/h$ and it evolved to a hydraulic jump perpendicular to the flow direction when the discharge increased to $9.01\,m^3/h$. Downstream this hydraulic jump, a complex wave structure was observed with different transverse shock waves, as in the previous geometry G1. A symmetrical wake appeared again downstream the obstacle tail but the observed oblique shock waves on both sides of the centered obstacle were weaker for this configuration.

The numerical results (Figure 13-right) showed an acceptable agreement with the observed flow structure for both discharges. Although the computational model was able to capture the transverse waves downstream the obstacle front face, important differences were found in the flow configuration upstream the obstacle. Actually the numerical discontinuities were somehow exaggerated when compared to those observed experimentally. With a discharge of $5.05\,m^3/h$ the numerical model predicted a oblique hydraulic jump upstream the obstacle but when discharge was increased to $9.01\,m^3/h$ the numerical result did not show its evolution to a perpendicular hydraulic jump as it was observed in the Kinect measurement.

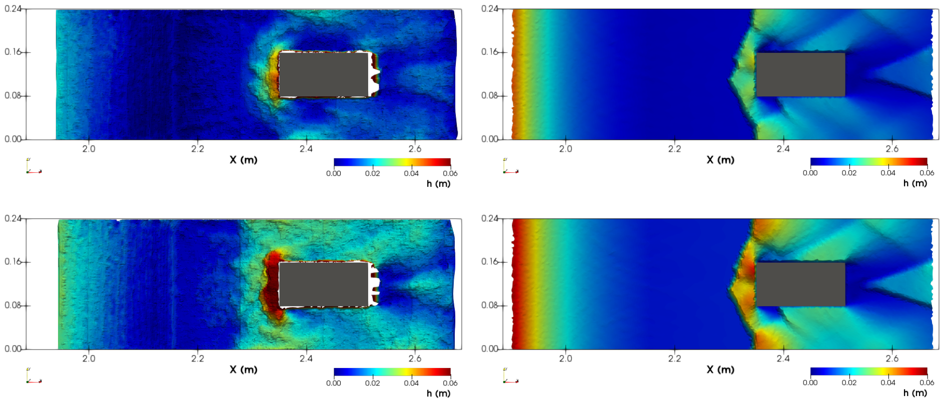

Figure 13: Experimental (left) and numerical (right) water depth 2D-fields for (top row) G2-S.1 and (bottom row) G2-S.2 cases.

The comparison of measured and computed water depth along the longitudinal flume center axis ($Y = 0.12\,m$) and the cross-section at $X = 2.40\,m$ is depicted in Figure 14 for both flow cases S.1 and S.2. Longitudinal water depth profiles at the flume center axis show a good agreement for experimental and simulated data except near the obstacle, whereas more significant differences appeared in the cross-section profile. These differences can be produced by the combination of shading areas and high slope water surfaces, as it was stated for the previous steady cases. It is interesting to note that the experimental cross-sectional profile for $Q_1 = 5.05\,m^3/h$ shows an exponential behaviour, whereas the numerical solution exhibits a logarithmic behaviour, suggesting wall-effects which are not captured in the model. However, the relative differences between numerical and experimental water depth (normalized by the mean flow depth upstream the floor bump) remained always below 20% far from the obstacle faces (Figure 15). Close to the obstacle's upstream face, the relative difference was more marked due to the disagreement in the hydraulic jump shape and height.

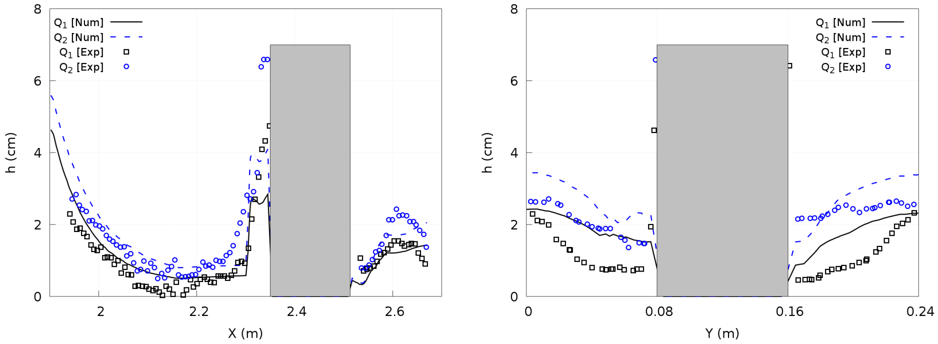

Figure 14: Experimental (dotted lines) and numerical (solid lines) water depth for steady cases with geometry G2: (left) longitudinal profile at Y = 0.12 m and (right) cross-section at X = 2.40 m.

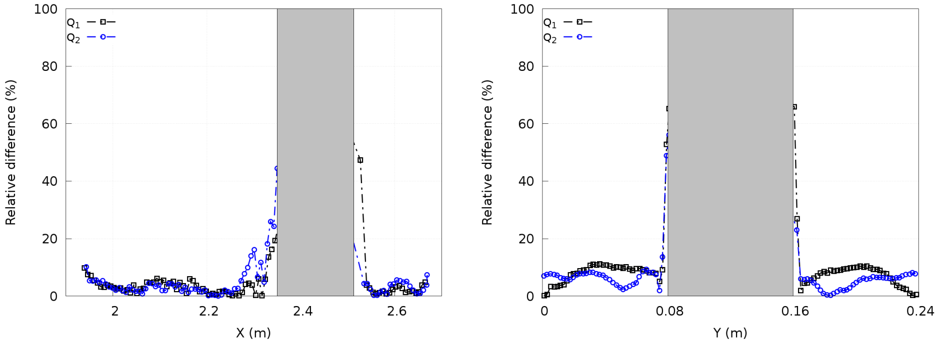

Figure 15: Relative differences between experimental and numerical water depth for steady cases with geometry G2: (left) longitudinal profile at Y = 0.12 m and (right) cross-section at X = 2.40 m.

4.3.2. Dam-break flow - Case G2-D.2

A dam-break with initial water depth upstream the gate of $h_0 = 13.0\ cm$ above the flume bed was tested with this geometry. Figure 16 shows a time sequence of the measured two-dimensional water depth field (left column) and the corresponding numerical results (right column). The supercritical dam-break wave overcame the bed bump with a high velocity and reached the centered obstacle at $t \approx 1.6 - 1.8\ s$. A strong shock wave appeared immediately at the front of the obstacle, exceeding its height and running over it ($t = 2.153 - 2.755\ s$). Then, this shock wave reduced its height and evolved to a hydraulic jump perpendicular to the main flow direction upstream the centered obstacle ($t = 3.527 - 5.512$ s). Simultaneously, a clear wake appeared downstream the obstacle.

The numerical model was able to correctly predict the arrival time of the dam-break wave and the main flow structure created around the centered obstacle, but some differences appeared in terms of the wave time progress. Although in general the computed and experimental results showed a good agreement, the numerical model demonstrated to suffer difficulties to accurately reproduce the flow over the obstacle as observed in the experiment, underestimating the frontal shock wave height. This is justified by the possible loss of validity of the shallow water approximation in this case. It neither predicted the position of the hydraulic jump properly. This may be due to the high velocity of water upon impact and the consequent three-dimensionality of flow during the impact. The wave arrival process in this case was more kinetic and violent than in previous cases.

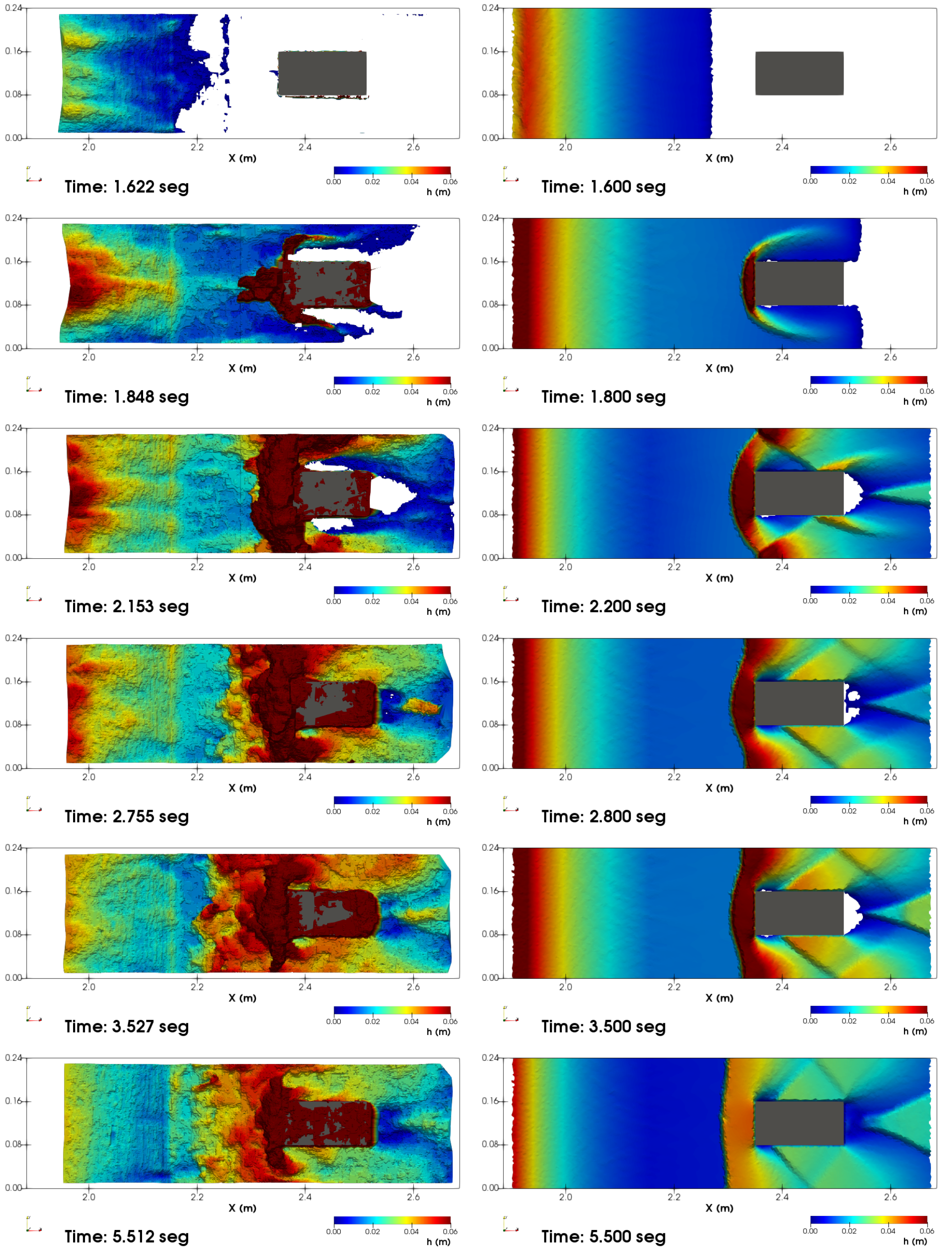

Figure 16: Experimental (left column) and numerical (right column) water depth 2D-fields for case G2-D.1 at different times.

Figure 17 shows the water depth temporal evolution along both the longitudinal flume center axis ($Y = 12\ cm$) and the longitudinal profile equidistant from the left flume wall and the left face of the obstacle ($Y = 20\ cm$). Differences in water depth can be found between numerical and observed values, especially for the frontal shock wave height and the hydraulic jump position. The profiles confirm that the shock develops into a vertical column which cannot be reproduced by the 2D simulations. This column later collapses into a standing wave. As the process evolves, and the initial violent impact effects disappear, the model performs increasingly better.

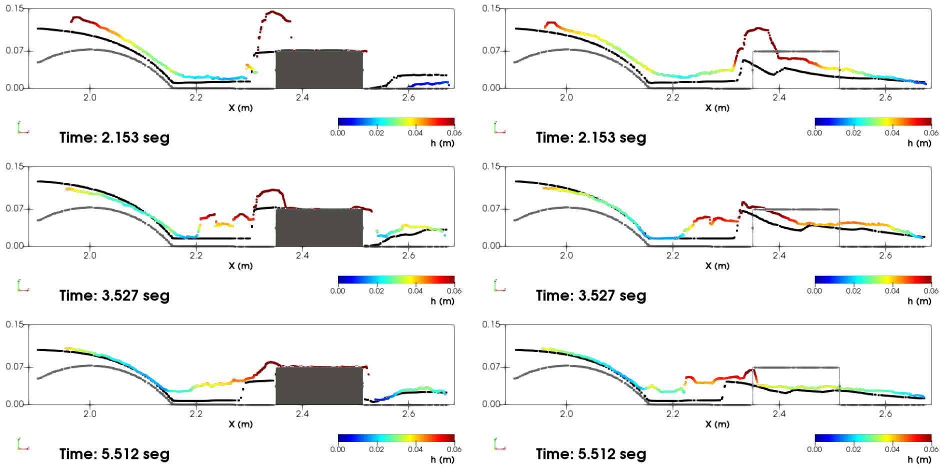

Figure 17: Experimental (colored line) and numerical (black line) free-surface longitudinal profiles for case G2-D.1 at different times: (left column) Y = 12 cm and (right column) Y = 20 cm. Grey color line represent the bed bump.

4.4. Venturi narrowing and centered obstacle (G3)

4.4.1. Steady flow - Cases G3-S.1 and G3-S.2

For the geometry G3, two different constant discharges were again set in the flume ($Q_1 = 5.05\, m^3/h$ and $Q2 = 9.01\, m^3/h$). Experimental time-averaged water depth fields are depicted in Figure 18-left. The flow was subcritical upstream the Venturi narrowing for both tested discharges and it became supercritical downstream the throat. A steady hydraulic jump with an upstream-concave shape appeared downstream the narrowing, changing again to subcritical regime before the flow reached the obstacle. Downstream the obstacle, the free surface developed a complex wave structure as with the previously reported geometries. The experimental flow field width reduction observed upstream the Venturi region was caused by visual shadowing zones created by the narrowing-pieces. The numerical model (Figure 18-right) was able to predict the observed flow structure including the position of the hydraulic jump in the narrow region (although some differences were found in the jump through) and the complex downstream wave structure.

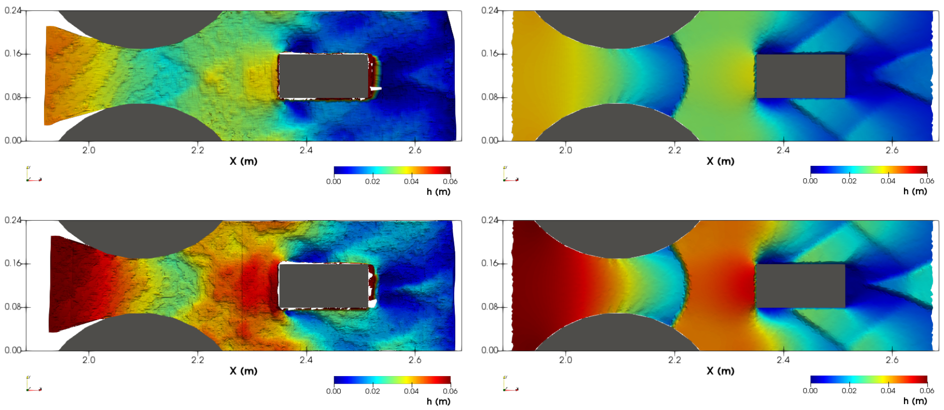

Figure 18: Experimental (left column) and numerical (right column) water depth 2D-fields for (top row) G3-S.1 and (bottom row) G3-S.2 cases.

A comparison of measured and computed water depth along the longitudinal flume center axis ($Y = 0.12\,m$) and cross-section at $X = 2.40\,m$ is depicted in Figure 19. The experimental and computed water depth values agree well for the longitudinal flume center profile, including the hydraulic jump height and position, as well as the diamond wake depth. The relative differences between observed and computed water depth (normalized by the mean flow depth upstream of the Venturi) remained always below 20% (Figure 15), except for the hydraulic jump through where the mismatch in the jump position between numerical and experimental results lead to very local higher differences. Finally, the measured and computed water depth along the cross-section at $X = 2.40\,m$ also showed an acceptable agreement with relative water depth differences below 20%. Once again, the overestimation of water depth by the numerical simulation in the cross-sectional profiles near the obstacle, suggests that significant wall-effects near the obstacle are not represented properly in the model.

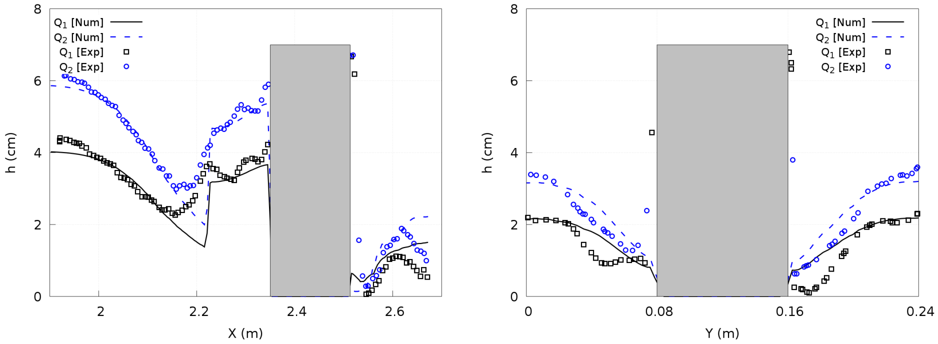

Figure 19: Experimental (dotted lines) and numerical (solid lines) water depth for steady cases with geometry G3: (left) longitudinal profile at Y = 0.12 m and (right) cross-section at X = 2.40 m.

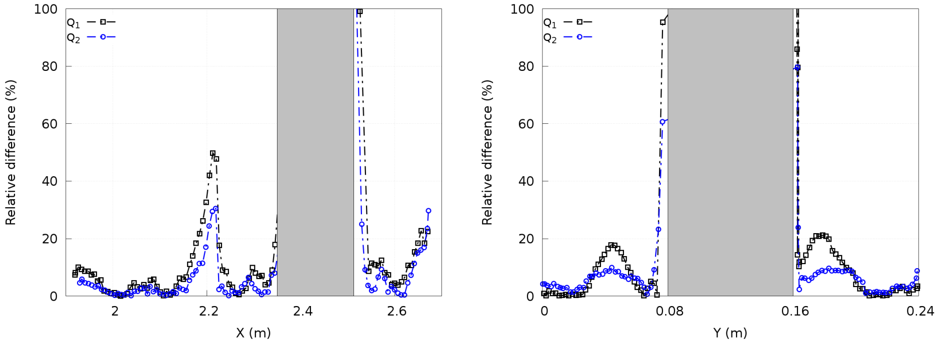

Figure 20: Relative differences between experimental and numerical water depth for steady cases with geometry G3: (left) longitudinal profile at Y = 0.12 m and (right) cross-section at X = 2.40 m.

4.4.2. Dam-break flow - Case G3-D.1

A dam-break case with an initial water depth upstream the boundary gate of $h_0 = 5.5\ cm$ was performed in the flume. Figure 21 shows a time sequence of the 2D water depth field for the Kinect data (left column). The supercritical dam-break wave reached the centered obstacle at approximately $t \approx 2.3\ s$. A shock wave appeared upstream the obstacle as in the previous cases, increasing with time and taking a curved shape ($t = 2.729 - 2.995\ s$), concave in the downstream direction. The free surface elevation increased upstream the central point of the Venturi narrowing. The downstream part of the shock wave resulted in a diagonal pattern, whereas the upstream part of the shock wave evolved upstream and developed an upstream concave curvature as time increased ($t = 3.416 - 3.853\ s$) forming a curved hydraulic jump downstream the central point of the narrowing ($t = 5.756\ s$). At this point the flow field acquired a similar structure as in the steady cases.

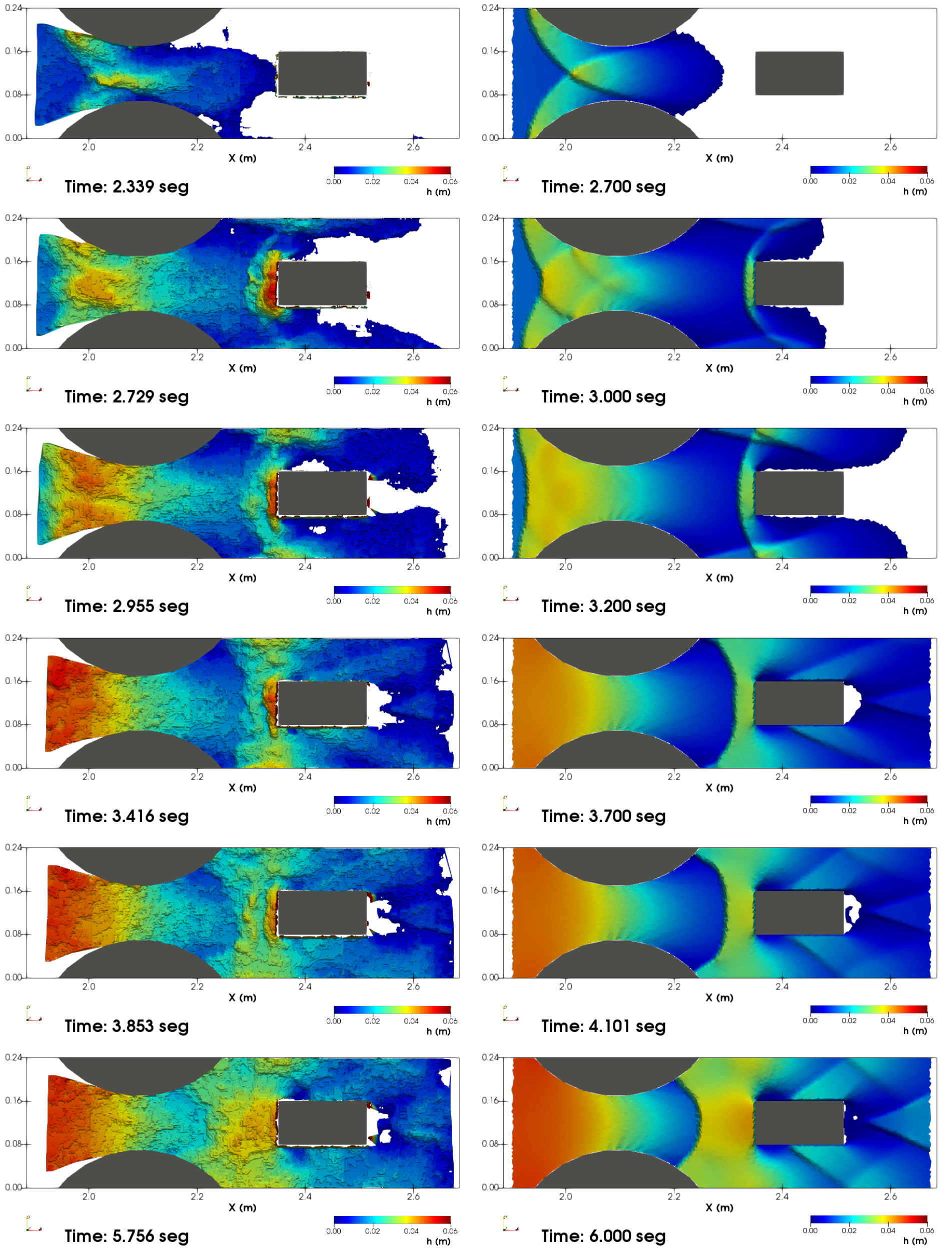

Figure 21: Experimental (left column) and numerical (right column) water depth 2D-fields for case G3-D.1 at different times.

Figure 21 (right column) shows the computed results for that transient flow. The numerical model was able to predict accurately all the free surface structures and the flow evolution, although the exact position of the structures was not perfectly reproduced. Nevertheless, a delay of 200-300 ms for the numerically computed flow evolution respect to that measured by the RGB-D sensor was observed for this case. Such delay could be caused by the difficulty to match the actual gate-opening instant and the initial time extracted from the Kinect images (even a delay of around $\sim 200\,ms$ could be possible). This must be taken into account when comparing experimental and numerical plots in Figure 21.

The water depth temporal evolution along both the longitudinal flume center axis ($Y = 12\ cm$) and the longitudinal profile at $Y = 20\ cm$ are shown in Figure 22. The numerical water depth profiles showed again a good agreement with the RGB-D sensor data, including the position of the hydraulic jump upstream the centered obstacle.

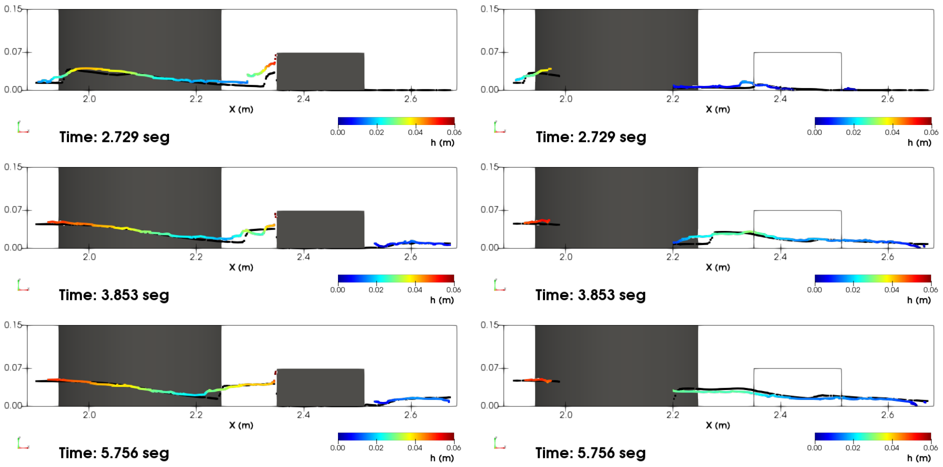

Figure 22: Experimental (colored line) and numerical (black line) free-surface longitudinal profiles for case G3-D.1 at different times: (left column) Y = 12 cm and (right column) Y = 20 cm. Initial time from the experimental measurements.

4.5. Two-arch bridge with downstream obstacles (G4-S.1)

Finally, a case with more complex geometry was carried out by placing a two-arch bridge linked to a centered longitudinal element which separated the flow out of each bride arch. In addition, a second obstacle was placed oblique to the flow direction and adjacent to the flume wall in order to perturb the flow out of the left arch. The inflow was set to 5.75 m^3/h, ensuring that the water level remained below the arch top point. This fact was important to ensure that the hypothesis of flow under hydrostatic pressure was still acceptable and hence the shallow water mathematical model remained applicable. Flow upstream the bridge was subcritical and became supercritical downstream. Moreover, the obstacles position and orientation caused a complex, non-symmetrical flow structure downstream the bridge, with a high degree of interaction between shock and rarefaction waves. Figure 23 shows the 2D water depth field obtained by the RGB-D sensor (left) and computed (right) for this steady case. Note that experimental data were not acquired in the arch due to the presence of the bridge top board.

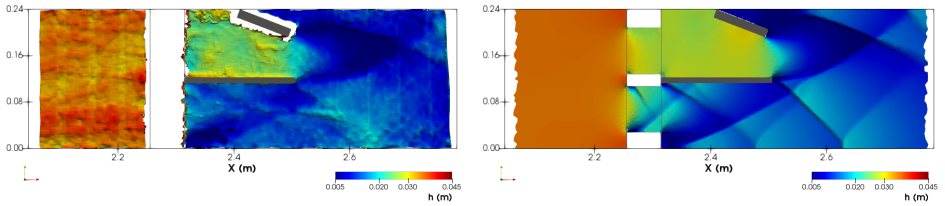

Figure 23: Experimental (left column) and numerical (right column) water depth 2D-fields for case G4-S.1.

The numerical model was able to predict the measured flow structure in both regions separated by the centered longitudinal piece, including both the backwater effect in the left arch and the complex wave interaction downstream the right arch. The right arch region is numerically challenging due to the elevated number of involved waves and the low flow depth. In order to perform a 2D spatial comparison of the flow structure, the Froude number field was computed from numerical results (note that this is not possible to do from experimental results, since the velocity field was not measured) and is shown in 24 (left panel). The gradient of the Froude field was computed and the regions with highest local gradient were identified –which correspond to shock wave regions– and are superimposed on the experimental depth field reported in figure 24 (right panel). The figure shows that the simulated shock wave structure agrees well with the experimental flow field, although some differences were found. Shock wave angles and curvatures are well reproduced. A small mismatch is observed downstream the oblique and longitudinal obstacles, in the low-depth region $(2.5 \leq X \leq 2.7, 0.12 \leq Y \leq 0.24)$.

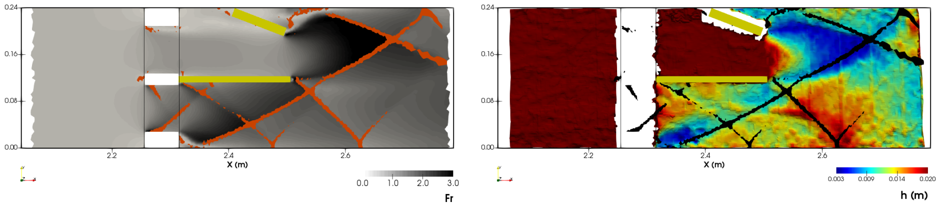

Figure 24: Computational Froude number (left) and experimental water depth (right) for case G4-S.1.

Furthermore, Figure 25-left shows measured and computed water depth along the longitudinal profile at $Y = 0.07\,m$ (centerline of right arch) and $Y = 0.165\,m$ (centerline of left arch). The experimental and computed water depth values along these longitudinal profiles agree well. The longitudinal profile at $Y = 0.165\,m$ allows to clarify the slight differences in the shock-wave structure, as simulated results show a sharper shock at $X \sim 2.65\,m$ than experimental results. The relative water depth difference (normalized by the mean water depth upstream the bridge) along these two longitudinal sections is also displayed in Figure 25-right, remaining always below 20%.

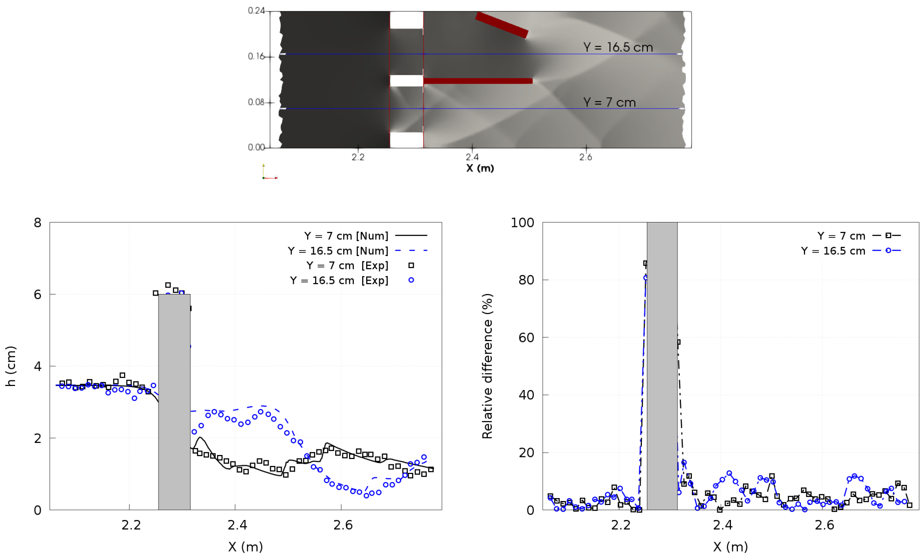

Figure 25: Longitudinal section location (top row), experimental and numerical water depth along the longitudinal sections (bottom left) and relative water depth differences (bottom right) for case G4-S.1.

5. Conclusions

The results of a laboratory-scale experimental campaign including steady and unsteady 2D water surfaces ranging from steady transcritical flow to dam-break flows around obstacles in a plexiglas flume have been presented. This work constitutes a new benchmarking dataset in which 2D transient water surfaces are available for shallow water model developers and users to further test and challenge these models. This dataset has been acquired by a novel use of commercial-grade RGB-D sensing devices which allows to capture a succession of 3D color-coded point clouds and construct the 2D free-surface elevation field for each measurement. The result is a novel collection of 2D benchmark shallow flow cases, with transient water depth and water elevation data for the entire visible flow field, allowing for qualitative and quantitative spatio-temporal comparisons with numerical simulations. We show that this technology is cost-effective and accurate for the purposes it was intended in this work, opening the way for further more complex applications for capturing experimental benchmarks for models and other applications of flume measurements. The main limitations of the experimental approach are technical, in terms of a limited field-of-view, thus requiring more sensors accurately positioned to cover a larger flume or basin with no shading areas, perhaps even with non-parallel optical axises, and the need to create an opaque water volume. Because of the low cost of the sensors –arguably their main advantage– together with their off-the-shelf operation makes a multi-sensor setup quite feasible.

This new 2D transient data can help identify limitations in the current generation of solvers, thus laying the ground for improvements in the near future. In consequence, simulations performed with an extensively-tested, state-of-the-art 2D shallow-water numerical model were performed and compared against the experimental data. The results show the suitability of this dataset for benchmarking purposes. Furthermore, the tested solver performed well even for complex transient flows. Spatial comparisons of flow structures were performed, and the high spatio-temporal resolution of the experimental and numerical data set allows to identify potential shortcomings in the numerical model. Such shortcoming is perhaps local friction effects around obstacles, suggesting a need for further mesh refinement and/or better friction calibration or representation. The comparisons also show that numerical results are much sharper at shock waves and much smoother elsewhere than the experimental results. This behaviour is a mix of the turbulent, chaotic behaviour in the experiment which is not represented in the model together with experimental uncertainty.

The methods and results here presented should be useful for the shallow-water community to further validate numerical solvers under more strenuous tests. Since the technology and methods are inexpensive and relatively straightforward, this work paves the way to performing more complex flow cases, for example in 2D basins with complex terrain, or including further processes such as moving beds and sediment transport.

Acknowledgements

This work was partially funded by the MINECO/FEDER under research project CGL2015-66114-R and by Diputacion General de Aragon, DGA, through Fondo Europeo de Desarrollo Regional, FEDER. The experimental data set is available in http://fiona.cps.unizar.es/~ghcuser/Kinect_exp_data.zip

References

[1] R. Hinkelmann, Q. Liang, V. Aizinger, C. Dawson, Robust shallow water models, Environ Earth Sci 74 (11) (2015) 7273–7274.

[2] P. García-Navarro, Advances in numerical modelling of hydrodynamics workshop, university of sheffield, UK, March 24-25, 2015, Applied Mathematical Modelling 40 (17-18) (2016) 7423.

[3] I. MacDonald, M. J. Baines, N. K. Nichols, P. G. Samuels, Analytic benchmark solutions for open-channel flows, Journal of Hydraulic Engineering 123 (11) (1997) 1041–1045.

[4] J. Murillo, P. García-Navarro, Augmented versions of the HLL and HLLC Riemann solvers including source terms in one and two dimensions for shallow flow applications, Journal of Computational Physics 231 (20) (2012) 6861 – 6906.

[5] O. Delestre, C. Lucas, P. Ksinant, F. Darboux, C. Laguerre, T. Vo, F. James, S. Cordier, Swashes: a compilation of shallow water analytic solutions for hydraulic and environmental studies, International Journal for Numerical Methods in Fluids 72 (3) (2013) 269–300.

[6] J. Fernández-Pato, M. Morales-Hernández, P. García-Navarro, Implicit finite volume simulation of 2d shallow water flows in flexible meshes, Computer Methods in Applied Mechanics and Engineering 328 (2018) 1 – 25.

[7] M. J. Briggs, C. E. Synolakis, G. S. Harkins, D. R. Green, Laboratory experiments of tsunami runup on a circular island, pure and applied geophysics 144 (3) (1995) 569–593.

[8] L. Fraccarollo, E. F. Toro, Experimental and numerical assessment of the shallow water model for two-dimensional dam-break type problems, Journal of Hydraulic Research 33 (6) (1995) 843–864.

[9] J. Hiver, Adverse-slope and slope (bump), in: S. Soares-Frazão, M. Morris, Y. Zech (Eds.), Concerted Action on Dam Break Modelling: Objectives, Project Report, Test Cases, Meeting Proceedings, Vol. CD-ROM, Université Catholique de Louvain, Civil Engineering Department, Hydraulics Division, Louvain-la-Neuve, Belgium, 2000.

[10] G. Testa, D. Zuccalà, F. Alcrudo, J. Mulet, S. Soares-Frazão, Flash flood flow experiment in a simplified urban district, Journal of Hydraulic Research 45 (sup1) (2007) 37–44.

[11] S. Soares-Frazão, Y. Zech, Experimental study of dam-break flow against an isolated obstacle, Journal of Hydraulic Research 45 (sup1) (2007) 27–36.

[12] P. Liu, H. Yeh, C. Synolakis, Advances in Coastal and Ocean Engineering, vol. 10, World Scientific, 2008, Ch. Advanced Numerical Models for Simulating Tsunami Waves and Runup.

[13] S. Soares-Frazão, Y. Zech, Dam-break flow through an idealised city, Journal of Hydraulic Research 46 (5) (2008) 648–658.

[14] H. Ozmen-Cagatay, S. Kocaman, H. Guzel, Investigation of dam-break flood waves in a dry channel with a hump, Journal of Hydro-environment Research 8 (3) (2014) 304 – 315.

[15] H. Ratia, J. Murillo, P. Garca-Navarro, Numerical modelling of bridges in 2d shallow water flow simulations, International Journal for Numerical Methods in Fluids 75 (4) (2014) 250–272.

[16] S. Kocaman, H. Ozmen-Cagatay, Investigation of dam-break induced shock waves impact on a vertical wall, Journal of Hydrology 525 (2015) 1–12.

[17] M. Velickovic, Y. Zech, S. Soares-Frazão, Steady-flow experiments in urban areas and anisotropic porosity model, Journal of Hydraulic Research 55 (1) (2016) 85–100.

[18] J.-M. Hervouet, A. Petitjean, Malpasset dam-break revisited with two-dimensional computations, Journal of Hydraulic Research 37 (6) (1999) 777–788.

[19] D. Caviedes-Voullième, P. García-Navarro, J. Murillo, Influence of mesh structure on 2d full shallow water equations and scs curve number simulation of rainfall/runoff events, Journal of Hydrology 448-449 (2012) 39 – 59.

[20] J. Fernández-Pato, D. Caviedes-Voullième, P. García-Navarro, Rainfall/runoff simulation with 2d full shallow water equations: Sensitivity analysis and calibration of infiltration parameters, Journal of Hydrology 536 (2016) 496 – 513.

[21] J. L. Carrivick, Dam break - outburst flood propagation and transient hydraulics: A geosciences perspective, Journal of Hydrology 380 (3-4) (2010) 338–355.

[22] J. L. Carrivick, R. Jones, G. Keevil, Experimental insights on geomorphological processes within dam break outburst floods, Journal of Hydrology 408 (1-2) (2011) 153–163.

[23] C. Juez, S. Soares-Frazao, J. Murillo, P. García-Navarro, Experimental and numerical simulation of bed load transport over steep slopes, Journal of Hydraulic Research 55 (4) (2017) 455–469.

[24] S. Soares-Frazão, R. Canelas, Z. Cao, L. Cea, H. M. Chaudhry, A. Die Moran, K. El Kadi, R. Ferreira, I. Fraga-Cadórniga, N. Gonzalez-Ramirez, M. Greco, W. Huang, J. Imran, J. Le Coz, R. Marsooli, A. Paquier, G. Pender, M. Pontillo, J. Puertas, B. Spinewine, C. Swartenbroekx, R. Tsubaki, C. Villaret, W. Wu, Z. Yue, Y. Zech, Dam-break flows over mobile beds: experiments and benchmark tests

for numerical models, Journal of Hydraulic Research 50 (4) (2012) 364–375.

[25] B. Spinewine, H. Capart, Intense bed-load due to a sudden dam-break, Journal of Fluid Mechanics 731 (2013) 579–614.

[26] C. Swartenbroekx, Y. Zech, S. Soares-Frazao, 2D Dam-break Flows over Erodible Floodplain. Comparison of Two Shallow-water Models against Laboratory Experiments: a Saint-Venant - Exner Classical Approach and a Two-layer Description, in: PROCEEDINGS OF THE 35TH IAHR WORLD CONGRESS, VOLS I AND II, TSINGHUA UNIV, 2013, pp. 4485–4494.

[27] L. Goutiere, S. Soares-Frazão, Y. Zech, Dam-break flow on mobile bed in abruptly widening channel: experimental data, Journal of Hydraulic Research 49 (3) (2011) 367–371.

[28] S. Creëlle, L. Engelen, L. Schindfessel, P. X. Ramos, T. De Mulder, Experimental investigation of free surface gradients in a 90° angled asymmetrical open channel confluence, in: P. Gourbesville, J. Cunge, G. Caignaert (Eds.), Advances in Hydroinformatics, Singapore, 2018, pp. 803–819.

[29] S. Kocaman, H. Ozmen-Cagatay, The effect of lateral channel contraction on dam break flows: Laboratory experiment, Journal of Hydrology 432-433 (2012) 145–153.

[30] I. Fent, Y. Zech, S. Soares-Frazão, Dam-break flow experiments over mobile bed: velocity profile, Journal of Hydraulic Research (2018) 1–8.

[31] M. Muste, A. Hauet, I. Fujita, C. Legout, H.-C. Ho, Capabilities of large-scale particle image velocimetry to characterize shallow free-surface flows, Advances in Water Resources 70 (2014) 160 – 171.

[32] A. M. Bento, S. Amaral, T. Viseu, R. Cardoso, R. M. L. Ferreira, Direct estimate of the breach hydrograph of an overtopped earth dam, Journal of Hydraulic Engineering 143 (6) (2017) 06017004.

[33] M. Wieland, J. Gray, K. Hutter, Channelized free-surface flow of cohesionless granular avalanches in a chute with shallow lateral curvature, Journal of Fluid Mechanics 392 (1999) 73.

[34] O. Pouliquen, Y. Forterre, Friction law for dense granular flows: application to the motion of a mass down a rough inclined plane, Journal of Fluid Mechanics 453 (2002) 133–151.

[35] D. Caviedes-Voullième, C. Juez, J. Murillo, P. García-Navarro, 2D dry granular free-surface flow over complex topography with obstacles. Part I: experimental study using a consumer-grade RGB-D sensor, Computers & Geosciences 73 (0) (2014) 177 – 197.

[36] P. Costabile, F. Macchione, Enhancing river model set-up for 2-d dynamic flood modelling, Environmental Modelling & Software 67 (0) (2015) 89 – 107.

[37] J. M. Daida, D. Lund, C. Wolf, G. A. Meadows, K. Schroeder, J. F. Vesecky, D. R. Lyzenga, B. C. Hannan, R. R. Bertram, Measuring topography of small-scale water surface waves, in: Geoscience and Remote Sensing Symposium, 1995. IGARSS '95. 'Quantitative Remote Sensing for Science and Applications', International, Vol. 3, 1995, pp. 1881–1883 vol.3.

[38] N. J. W. Morris, Image-based water surface reconstruction with refractive stereo, Master's thesis, Department of Computer Science, University of Toronto (2004).

[39] L. Engelen, S. Creëlle, L. Schindfessel, T. D. Mulder, Spatio-temporal image-based parametric water surface reconstruction: a novel methodology based on refraction, Measurement Science and Technology 29 (3) (2018) 035302.

[40] F. Evers, H. Hager, Videometric water surface tracking: towards investigating spatial impulse waves, in: 36th IAHR World Congress: Deltas of the Future and what happens upstream, 2015.

[41] L. Zou, Y. Qi, G. Wang, Advanced Multimedia and Ubiquitous Engineering, Springer, 2016, Ch. A Method of Image-Based Water Surface Reconstruction, pp. 437–443.

[42] F. Franzini, S. Soares-Frazao, H. Capart, Measurement of the free-surface elevation in a steady flow in complex topography using photogrammetry, in: River Flow 2016: Proceedings of the International Conference on Fluvial Hydraulics, 2016, pp. 581–587.

[43] O. C. d'Odeigne, F. Franzini, G. C. M. D. Rosa, N. Janssens, S. Soares-Frazão, Measurement of the free-surface elevation for flows in complex topography using photogrammetry, in: Advances in Hydroinformatics, Springer Singapore, 2018, pp. 145–156.

[44] F. Aureli, A. Maranzoni, P. Mignosa, C. Ziveri, An image processing technique for measuring free surface of dam-break flows, Experiments in Fluids 50 (3) (2010) 665–675.

[45] F. Aureli, S. Dazzi, A. Maranzoni, P. Mignosa, A combined colour-infrared imaging technique for measuring water surface over non-horizontal bottom, Experiments in Fluids 55 (3).

[46] L. Chatellier, S. Jarny, F. Gibouin, L. David, A parametric PIV/DIC method for the measurement of free surface flows, Experiments in Fluids 54 (3).

[47] G. Gomit, L. Chatellier, D. Calluaud, L. David, Free surface measurement by stereo-refraction, Experiments in Fluids 54 (6).

[48] I. Ng, V. Kumar, G. J. Sheard, K. Hourigan, A. Fouras, Experimental study of simultaneous measurement of velocity and surface topography: in the wake of a circular cylinder at low reynolds number, Experiments in Fluids 50 (3) (2010) 587–595.

[49] H. Du, P. Henry, X. Ren, M. Cheng, D. B. Goldman, S. M. Seitz, D. Fox, Interactive 3d modeling of indoor environments with a consumer depth camera, in: Proceedings of the 13th International Conference on Ubiquitous Computing, UbiComp '11, ACM, New York, NY, USA, 2011, pp. 75–84.

[50] A. S. Huang, A. Bachrach, P. Henry, M. Krainin, D. Maturana, D. Fox, N. Roy, Visual Odometry and Mapping for Autonomous Flight Using an RGB-D Camera, Springer International Publishing, Cham, 2017, pp. 235–252.

[51] K. Berger, M. Kastner, Y. Schroeder, S. Guthe, Using Sparse Optical Flow for Two-Phase Gas Flow Capturing with Multiple Kinect, Springer International Publishing, Cham, 2014, pp. 157–169.

[52] S. Izadi, D. Kim, O. Hilliges, D. Molyneaux, R. Newcombe, P. Kohli, J. Shotton, S. Hodges, D. Freeman, A. Davison, A. Fitzgibbon, Kinectfusion: Real-time 3d reconstruction and interaction using a moving depth camera, ACM, 2011, pp. 559–568.

[53] H. González-Jorge, B. Riveiro, E. Vázquez-Fernández, J. Martínez-Sánchez, P. Arias, Metrological evaluation of Microsoft Kinect and Asus Xtion sensors, Measurement 46 (6) (2013) 1800 – 1806.

[54] H. González-Jorge, P. Rodríguez-Gonzálvez, J. Martínez-Sánchez, D. González-Aguilera, P. Arias, M. Gesto, L. D.-V. no, Metrological comparison between kinect I and kinect II sensors, Measurement 70 (2015) 21 – 26.

[55] H. Sarbolandi, D. Lefloch, A. Kolb, Kinect range sensing: Structured-light versus time-of-flight kinect, CoRR abs/1505.05459.

[56] T. Stoyanov, R. Mojtahedzadeh, H. Andreasson, A. J. Lilienthal, Comparative evaluation of range sensor accuracy for indoor mobile robotics and automated logistics applications, Robotics and Autonomous Systems 61 (10) (2013) 1094–1105.

[57] R. Horaud, M. Hansard, G. Evangelidis, C. Ménier, An overview of depth cameras and range scanners based on time-of-flight technologies, Machine Vision and Applications 27 (7) (2016) 1005–1020.

[58] E. Lachat, H. Macher, T. Landes, P. Grussenmeyer, Assessment and calibration of a RGB-d camera (kinect v2 Sensor) towards a potential use for close-range 3D modeling, Remote Sensing 7 (10) (2015) 13070–13097.

[59] M. Hämmerle, B. Hofle, J. Fuchs, A. Schroder-Ritzrau, N. Vollweiler, N. Frank, Comparison of kinect and terrestrial LiDAR capturing natural karst cave 3-d objects, IEEE Geoscience and Remote Sensing Letters 11 (11) (2014) 1896–1900.

[60] B. Langmann, K. Hartmann, O. Loffeld, Depth camera technology comparison and performance evaluation, in: ICPRAM, 2012.

[61] C. Dal Mutto, P. Zanuttigh, G. M. Cortelazzo, Time-of-Flight Cameras and Microsoft Kinect, Springer, 2012.

[62] S. Kahn, U. Bockholt, A. Kuijper, D. W. Fellner, Towards precise real-time 3d difference detection for industrial applications, Computers in Industry 64 (9) (2013) 1115 – 1128.

[63] K. D. Mankoff, T. A. Russo, The Kinect: a low-cost, high-resolution, short-range 3D camera, Earth Surface Processes and Landforms 38 (9) (2013) 926–936.

[64] L. M. G. Guidi, S. Gonizzi, 3d capturing performances of low cost range sensors for mass market applications, in: The International Archives of the Photogrammetry, Remote Sensing and Spatial Information Sciences (XXIII ISPRS Congress), Vol. XLI-B5, 2016.

[65] T. Butkiewicz, Low-cost coastal mapping using kinect v2 time-of-flight cameras, in: 2014 Oceans - St. John's, 2014, pp. 1–9.

[66] G. M. Chávez, D. Sarocchi, E. A. Santana, L. Borselli, L. Rodríguez-Sedano, Using kinect to analyze pebble to block-sized clasts in sedimentology, Computers & Geosciences 72 (2014) 18–32.

[67] F. Marinello, A. Pezzuolo, F. Gasparini, J. Arvidsson, L. Sartori, Application of the kinect sensor for dynamic soil surface characterization, Precision Agriculture 16 (6) (2015) 601–612.

[68] L. M. Thomsen, J. E. M. Baartman, R. J. Barneveld, T. Starkloff, J. Stolte, Soil surface roughness: comparing old and new measuring methods and application in a soil erosion model, SOIL 1 (1) (2015) 399–410.

[69] K. Khoshelham, S. O. Elberink, Accuracy and resolution of kinect depth data for indoor mapping applications, Sensors 12 (2) (2012) 1437–1454.

[70] S. Paulus, J. Behmann, A.-K. Mahlein, L. Plümer, H. Kuhlmann, Low-cost 3D systems: Suitable tools for plant phenotyping, Sensors 14 (2) (2014) 3001–3018.

[71] M. Hämmerle, B. Höfle, Direct derivation of maize plant and crop height from low-cost time-of-flight camera measurements, Plant Methods 12 (1).

[72] Z. Wang, K. Walsh, B. Verma, On-tree mango fruit size estimation using RGB-d images, Sensors 17 (12) (2017) 2738.

[73] T. Dutta, Evaluation of the Kinect sensor for 3-D kinematic measurement in the workplace, Applied Ergonomics 43 (4) (2012) 645 – 649.

[74] K. Berger, K. Ruhl, M. Albers, Y. Schröder, A. Scholz, J. Kokemüller, S. Guthe, M. Magnor, The capturing of turbulent gas flows using multiple kinects, in: 2011 IEEE International Conference on Computer Vision Workshops (ICCV Workshops), 2011, pp. 1108–1113.

[75] B. Combes, A. Guibert, E. Mémin, D. Heitz, Free-surface flows from Kinect: Feasibility and limits, in: FVR2011, Poitiers, France, 2011, p. 4 p.

[76] A. Nichols, M. Rubinato, Remote sensing of environmental processes via low-cost 3d free-surface mapping, in: Proceedings of the 4th IAHR Europe Congress, 2016.

[77] F. Klopfer, M. Hämmerle, B. Höfle, Assessing the potential of a low-cost 3-d sensor in shallow-water bathymetry, IEEE Geoscience and Remote Sensing Letters 14 (8) (2017) 1388–1392.

[78] S. Chourasiya, P. Mohapatra, S. Tripathi, Non-intrusive underwater measurement of mobile bottom surface, Advances in Water Resources 104 (2017) 76 – 88.

[79] S. Amaral, T. Alvarez, V. T, R. Ferreira, Image analysis detection applied to dam breach experiments, in: 5th IAHR Europe Congress: New challenges in hydraulic research and engineering, 2018.

[80] A. Anwer, S. S. A. Ali, A. Khan, F. Meriaudeau, Underwater 3-d scene reconstruction using kinect v2 based on physical models for refraction and time of flight correction, IEEE Access 5 (2017) 15960–15970.

[81] A.-J.-C. Saint-Venant, Théorie du mouvement non permanent des eaux, avec application aux crues des rivires et à l'introduction des marées dans leur lit, Comptes rendus hebdomadaires des séances de l'Académie des sciences, France 73 (1871) 11 p.

[82] C. Vreugdenhil, Numerical Methods for Shallow Water Flow, Kluwer Academic Publishers, Dordrecht, The Netherlands, 1994.

[83] J. Murillo, P. García-Navarro, Weak solutions for partial differential equations with source terms: Application to the shallow water equations, Journal of Computational Physics 229 (2010) 4327–4368.

[84] J. Murillo, A. Navas-Montilla, A comprehensive explanation and exercise of the source terms in hyperbolic systems using Roe type solutions. application to the 1D-2D shallow water equations, Advances in Water Resources 98 (2016) 70 – 96.